

When Color meets Gravity; Near-Threshold Exclusive J/ψ Photoproduction on the Proton

B. Duran^{3,1}, Z.-E. Meziani^{1,3**}, S. Joosten¹, M. K. Jones², S. Prasad¹, C. Peng¹, W. Armstrong¹, H. Atac³, E. Chudakov², H. Bhatt⁵, D. Bhetuwal⁵, M. Boer¹¹, A. Camsonne², J.-P. Chen², M. Dalton², N. Deokar³, M. Diefenthaler², J. Dunne⁵, L. El Fassi⁵, E. Fuchey⁹, H. Gao⁴, D. Gaskell², O. Hansen², F. Hauenstein⁶, D. Higinbotham², S. Jia³, A. Karki⁵, C. Keppel², P. King⁶, H.S. Ko¹⁰, X. Li⁴, R. Li³, D. Mack², S. Malace², M. McCaughan², R. E. McClellan⁸, R. Michaels², D. Meekins², L. Pentchev², E. Pooser², A. Puckett⁹, R. Radloff⁵, M. Rehfuss³, P. E. Reimer¹, S. Riordan¹, B. Sawatzky², A. Smith⁴, N. Sparveris³, H. Szumila-Vance², S. Wood², J. Xie¹, Z. Ye¹, C. Yero⁶, and Z. Zhao⁴

List of affiliations*

ABSTRACT

The proton is one of the main building blocks of all visible matter in the universe¹. Among its intrinsic properties are its electric charge, mass, and spin². These emerge from the complex dynamics of its fundamental constituents, quarks and gluons, described by the theory of quantum chromodynamics (QCD)^{3–5}. Using electron scattering its electric charge and spin, shared among the quark constituents, have been the topic of active investigation until today. An example is the novel precision measurement of the proton's electric charge radius⁶. In contrast, little is known about the proton's inner mass density, dominated by the energy carried by the gluons, which are hard to access through electron scattering since gluons carry no electromagnetic charge. In the present work we chose to probe this gluonic gravitational density using a small color dipole, the J/ψ particle, through its threshold photoproduction. From our data we determined, for the first time, the proton's gluonic gravitational form factors^{7,8}, which encode its mass density. We used a variety of methods and determined in all cases a mass radius that is notably smaller than the electric charge radius. In some cases, the determined radius is in excellent agreement with first-principle predictions from lattice QCD⁹. This work paves the way for a deeper understanding of the salient role of gluons in providing gravitational mass to visible matter.

In the standard model of cosmology, after the big bang nucleosynthesis, most of the mass of the visible universe was encapsulated in protons, neutrons, and nuclei. In the preceding hadron epoch, the color-neutral confined systems, such as the proton and neutron, resulted from the interplay of strong color forces among the fundamental constituents, quarks and gluons. Surprisingly, emerging from this interplay is a total nucleon mass much larger than the constituents' mass sum. Thus, the origin of the proton mass is an essential puzzle piece in our understanding of the structure of visible matter in the universe¹. The triumphant discovery of the Higgs boson offered a crucial explanation for the origin of quark masses. However, the quarks are almost massless (few MeV) and account only for a tiny fraction of the total proton mass of about 1 GeV, even when accounting for their relativistic nature. Thus the question arises: How do the massless gluons provide the sizeable remaining mass of the

proton, and how is this mass distributed across the confinement size of the proton? While Einstein's original definition of the mass of a body, $m = E/c^2$ starts to answer this question, we can gain real insight through the measurement of the proton's gravitational form factors (GFFs) and the determination of the trace anomaly. GFFs are the matrix elements of the proton's energy-momentum tensor (EMT)^{7,8} and encode its mechanical properties, while the trace anomaly of the EMT is a key component of the origin of mass according to Quantum Chromodynamics (QCD)^{3–5}. Moreover, with the advent of lattice QCD, we can challenge and benchmark our understanding of the proton's internal structure with ab-initio calculations^{10–12}.

In the past 40 years, we have extensively investigated the electric charge and spin of the proton. For example, we learned how the proton charge and magnetization, carried by the electrically charged moving quarks, are distributed and

^{*}¹Argonne National Laboratory, Lemont, IL 60439, USA. ²Thomas Jefferson National Accelerator Facility, Newport News, VA 23606, USA. ³Temple University, Philadelphia, PA 19122, USA. ⁴Duke University, Durham 27708, NC, USA. ⁵Mississippi State University, Mississippi State 39762, MS, USA. ⁶Old dominion University, Norfolk 23529, VA, USA. ⁷Ohio University, Athens 45701, OH, USA. ⁸Pensacola State College, Pensacola, FL 32504, ⁹University of Connecticut, Storrs 06269, CT, USA. ¹⁰Université Paris-Saclay, Gif-sur-Yvette 91190, Essonne France. ¹¹Virginia Polytechnic Institute & State University, Blacksburg, VA 24061, USA. ^{**}corresponding author:zmeziani@anl.gov

determined the proton electric charge radius through elastic electron scattering⁶. In contrast, the description of the mass distribution of the proton, carried mainly by gluons and their color interactions, is a subject in its infancy: Gluons carry no charge and thus are not amenable to direct study using an electromagnetic probe.

Recently, it was suggested that measurements of the differential photoproduction of J/ψ cross-section in the threshold region as a function of the momentum transfer t offer a promising path to access the gluonic GFFs of the proton^{13–19}. The gluonic GFFs or EMT form factors provide information on the mass, pressure, and shear distributions of gluons in the proton⁷. With sufficient data at different photon energies, the slopes and magnitudes of the GFFs determined at $t = 0$ give access to the mass-radius and potentially to the matrix element of the trace anomaly of the energy-momentum tensor. The latter is the ultimate reason for the large nucleon mass carried by the gluonic fields. This work reports on a J/ψ photoproduction measurement in the threshold region performed in Hall C at Jefferson Lab. We present, for the first time, the measured t distributions of the cross sections as a function of the photon energy in the range of $9.1 \text{ GeV} \leq E_\gamma \leq 10.6 \text{ GeV}$ and explore the impact of our data on the determination of the GFFs, the proton mass-radius, and the trace anomaly²¹.

Our focus is the largely unknown gluonic GFFs, the mass and

scalar radii of the proton in relation to its charge radius, and the contribution of the trace anomaly to the proton mass²⁰.

The near threshold J/ψ photoproduction experiment, E12-16-007 a.k.a $J/\psi - 007$, was carried at Jefferson Lab between February 8th and March 5th, 2019. We measured the exclusive J/ψ photoproduction cross section, depicted in Fig. 1(a), in two dimensions as a function of the Mandelstam variable t and photon beam energy E_γ , covering the phase space shown in Fig. 1(b). We achieved this²² using a bremsstrahlung photon beam emitted from a 10.6 GeV electron beam while traversing an 8.5% radiation length Cu radiator positioned about 1 m upstream from the Hall C target chamber. The produced photon beam together with the electron beam passed through a target consisting of a 10 cm long cylinder-shaped aluminum can containing liquid hydrogen at 19°K temperature and 25 psi pressure. We measured the photoproduced J/ψ mesons in the energy range from $E_\gamma = 8.8 \text{ GeV}$ up to the bremsstrahlung endpoint energy of $E_\gamma = 10.6 \text{ GeV}$ as shown in Fig. 1(b). The e^-e^+ decay pair of the J/ψ was detected in coincidence using the two high momentum spectrometers of Hall C: the Super High Momentum Spectrometer (SHMS) and High Momentum Spectrometer (HMS) for the electron and the positron, respectively, as shown in Fig. 1(c).

In Fig. 2 we show the unfolded two-dimensional dif-

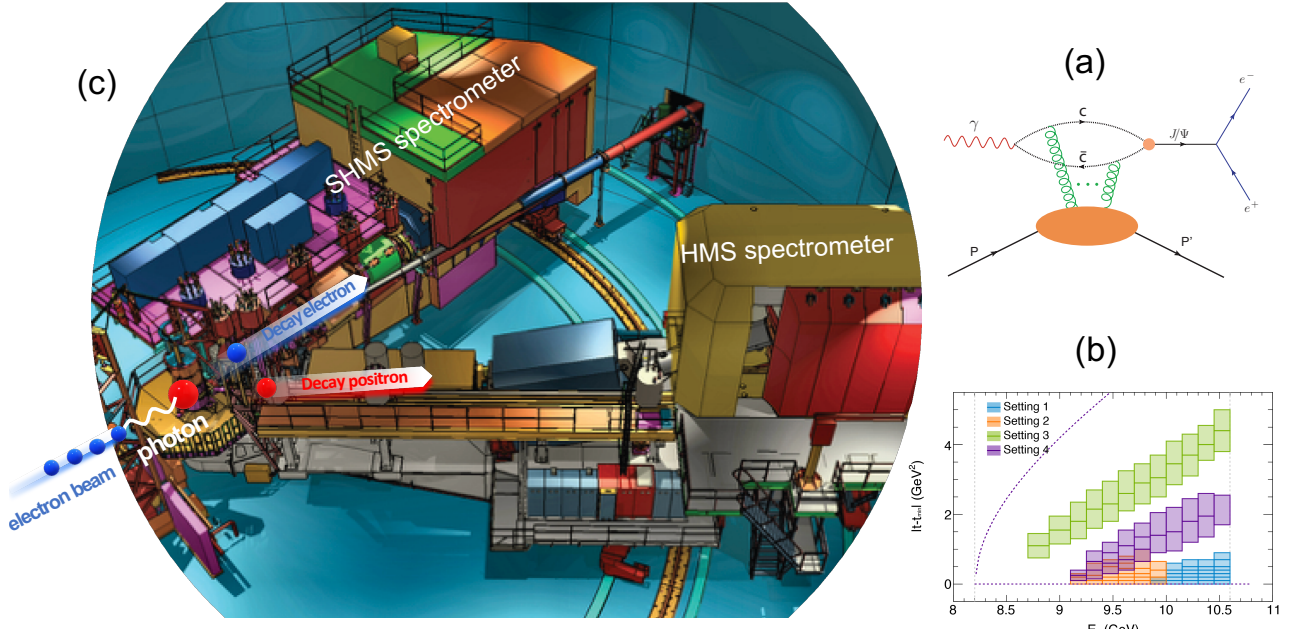


Figure 1. (a): Standard diagram for exclusive J/ψ photoproduction off a nucleon in the t -channel at large invariant mass. In the threshold region, the exchange involves multiple gluons configurations (denoted by '...'). For example, holographic QCD describes the process through tensor 2^{++} graviton-like exchange and scalar 0^{++} exchange. (b): Phase space $|t - t_{\min}|$ vs E_γ , covered in the experiment in four kinematic settings. The dash-dotted vertical lines mark the J/ψ threshold photon energy and the maximum beam energy, 10.6 GeV. The magenta dashed curves represent the limit values of $t = t_{\min}$ and $t = t_{\max}$. (c): Layout of the J/ψ -007 experiment in Hall C. A 10.6 GeV incident electron beam strikes a liquid hydrogen target after passing through an 8.5% Cu radiator. The resulting bremsstrahlung photon beam together with the incident electron beam produce J/ψ particles, which subsequently decay in e^+e^- pairs, detected in coincidence with the HMS and SHMS spectrometers.

ferential cross-sections, where each panel corresponds to a different central photon energy with a bin width of 150 MeV. The data are presented together with a dipole fit (solid black line) according to Ref.¹³ and its corresponding uncertainty band (gray shaded area). Also shown is a comparison of the data to the calculations described in references^{13–17,19} where each model parameters were already published and fixed using the GlueX³⁰ results at an average photon beam energy of 10.72 GeV with a range from 10 GeV to 11.8 GeV. At photon energies close to the GlueX average photon energy, all models seem to reproduce our data reasonably well but tend to deviate from the data at photon energies below 9.55 GeV, closer to threshold. One exception is the holographic predictions of Ref.¹⁷ which seems to track the change in the t slope observed in the data.

In order to take advantage of our two dimensional results, we expanded our analysis to fit our cross sections using to two approaches that explicitly use two GFFs, $A_g(t)$ and $C_g(t)$, in the cross section calculations. Here we assumed that $B_g(t)$'s contribution is small^{9,23}. We used both the holographic and general parton distribution (GPD) approaches to describe the cross sections to extract the $A_g(t)$ and $C_g(t)$ form factors and deduce *one* mass radius and *one* scalar radius.

In the holographic QCD calculation of ref.^{23,24} (labeled M-Z), the dominant exchange is associated with a graviton-like exchange (quantum numbers 2^{++}), however a dilaton-like exchange contribution (quantum numbers 0^{++}) is also included. Both the $A_g(t)$ and $C_g(t)$ form factors are used in the differential cross section expression. While these gravitational form factors have a well defined expression^{23,24} in the holographic calculation, dipole approximations inspired from the latest lattice calculations ref.⁹ are used. In our M-Z fitting procedure, the GFFs are parameterized with a total of three unknown parameters, m_T for the dipole form of $A_g(t)$, and $C_g(t=0)$ and m_S for the dipole form of $C_g(t)$. The fourth parameter, $A_g(t=0)$, is related to the momentum fraction carried by the gluons in the proton, a value that is well-constrained by the experimental data on deep-inelastic scattering. We fixed $A_g(t=0)$ to the value obtained from the CT18 global fit²⁵ $\langle x \rangle_g = 0.414 \pm 0.008$. Values from other contemporary global fits were also considered, and were found to be consistent within one sigma of their uncertainty. Furthermore, it is worth noting that the CT18 value of $\langle x \rangle_g$ agrees well with different lattice calculations^{9,26,27}, albeit with a better uncertainty.

In the GPD approach of ref.¹⁴, the authors used two GFFs $A_g(t)$ and $C_g(t)$ of a dipole form, fixed the $A_g(0)$ and m_C parameters to lattice²⁸ and used the VMD model to connect the forward scattering amplitude of $J/\psi N \rightarrow J/\psi N$ to that of $\gamma N \rightarrow J/\psi N$. In this work, as described in previously, we chose dipole forms for both $A_g(t)$ and $C_g(t)$ while fixing $A_g(t=0)$ to the value from CT18 pdfs extraction. We then proceeded to determine m_A , m_C , and $C(t=0)$ by performing a two dimensional fit to our data.

In Fig. 3 both the $A_g(k^2)$ and $C_g(k^2)$ gluonic GFFs

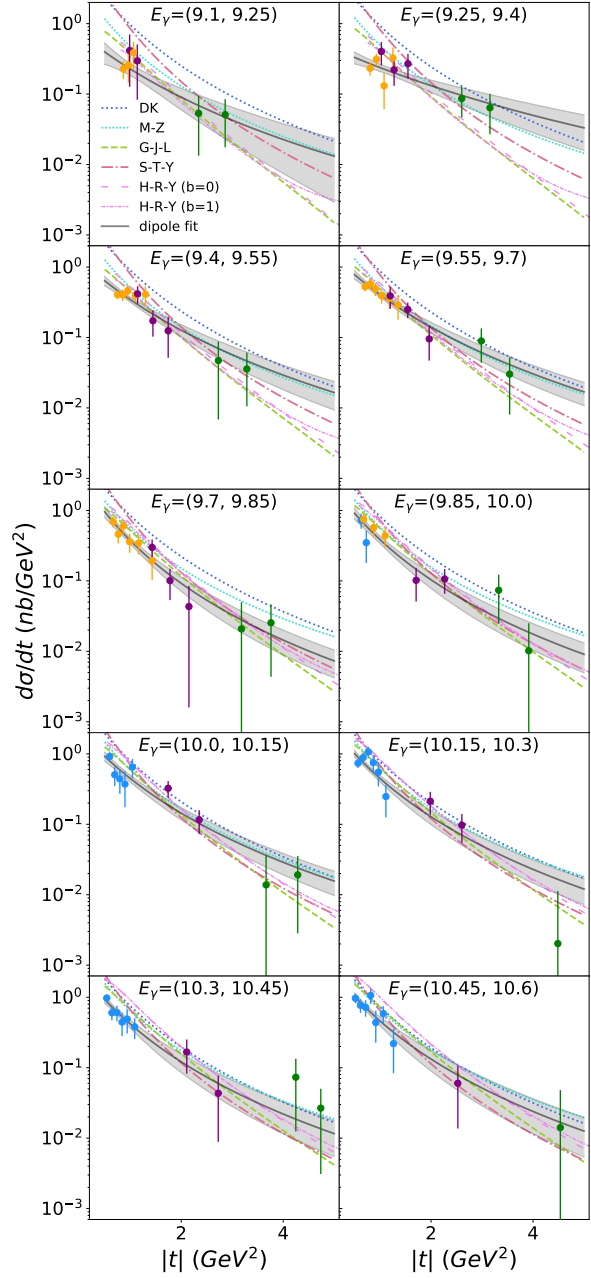


Figure 2. Differential cross sections versus $|t|$. The color of the data points indicates the experimental setting matching the color scheme in Fig. 1(b). Each panel shows a different photon energy in GeV with 0.150 GeV bin size. The black solid curve is a dipole fit to our data according to ref.¹³ and the grey band shows its uncertainty. The parameters are listed in Table 3. Every other curve is a prediction with fixed parameters determined from the GlueX results. Blue dotted line (labeled DK) uses¹³, black dotted line (labeled M-Z) is the holographic QCD approach²³, green dashed line (labeled G-J-L) is the GPD+VMD approach¹⁴, red-dash-dotted line is a higher twist approach (labeled S-T-Y)¹⁹, and finally purple dash (purple dash-dot) labeled H-R-Y is another holographic calculation^{15,16,29} with maximal (minimal) trace anomaly contribution to the EMT matrix element.

extracted from our two-dimensional cross section data, within the holographic and GPD+VMD approaches, are compared to the latest lattice calculation from ref.⁹, where $k^2 \equiv |t|$. For the $A_g(k^2)$ form factor (top panel), the GPD+VMD approach results in a form factor that is larger over the entire t -range than both the holographic QCD or lattice result. Our data clearly expand the t range up to 4.5 GeV^2 , doubling the range of $|t|$ compared the lattice calculations or extractions from the one-dimensional GlueX results³⁰. Furthermore, the two-dimensional nature of our results allow, for the first time, to simultaneously constrain all three unknown parameters, m_A , m_C and $C(t = 0)$, from experimental data. The $A_g(t)$ GFF extracted using the holographic QCD approach agrees well with the lattice results, hinting that this approach may provide a path for extracting the gluonic GFFs in this non-perturbative region of J/ψ threshold production.

Finally, after determining the gluonic GFFs in the holographic QCD and GPD+VMD approaches, the proton mass and scalar radii can be deduced according to the expressions of¹⁴, respectively,

$$\langle r_m^2 \rangle_g = 6 \frac{1}{A_g(0)} \frac{dA_g(t)}{dt} \Big|_{t=0} - 6 \frac{1}{A_g(0)} \frac{C_g(0)}{M_N^2} \quad (1)$$

$$\langle r_s^2 \rangle_g = 6 \frac{1}{A_g(0)} \frac{dA_g(t)}{dt} \Big|_{t=0} - 18 \frac{1}{A_g(0)} \frac{C_g(0)}{M_N^2} \quad (2)$$

where M_N is the nucleon mass. Table 1 shows the extracted parameters that define the gluonic GFFs for each of the holographic and GPD+VMD approach together with the corresponding mass and scalar radius determined using eqs.(1,2). We also report the lattice values for comparison. The radii extracted following the holographic QCD approach, which agree well with the lattice results, suggest a three-fold nucleon structure, with a mass radius smaller than the charge radius and a scalar radius extending well beyond the charge radius, about one fermi.

For completeness we also carried out a one-dimensional analysis of our results to determine the mass radius according to the VMD-based approach from ref.¹³ (labeled DK), for each photon energy separately. Additionally, following the VMD approach described in refs.^{13,37-39}, we extracted the anomalous mass contribution to the proton mass M_A/M comparing an exponential GFF (as in ref.³⁹) to a a dipole form GFF (as in ref.¹³). This analysis is discussed in the supplemental material.

We have measured the exclusive J/ψ photoproduction differential cross sections near threshold as a function of photon energy E_γ from 9.1 GeV to 10.6 GeV , and four-momentum transfer t from t_{min} up to 4.5 GeV^2 . We fit our two-dimensional data using the cross section expressions from the holographic QCD approach²³ and the GPD+VMD approach¹⁴ to fully determine, for the first time, the gluonic GFFs $A_g(t)$ and $C_g(t)$ from purely experimental data, up to $|t| = 4.5 \text{ GeV}^2$. We found $D(t) = 4C(t)$ to be negative over the measured t -range. We compared our extracted results

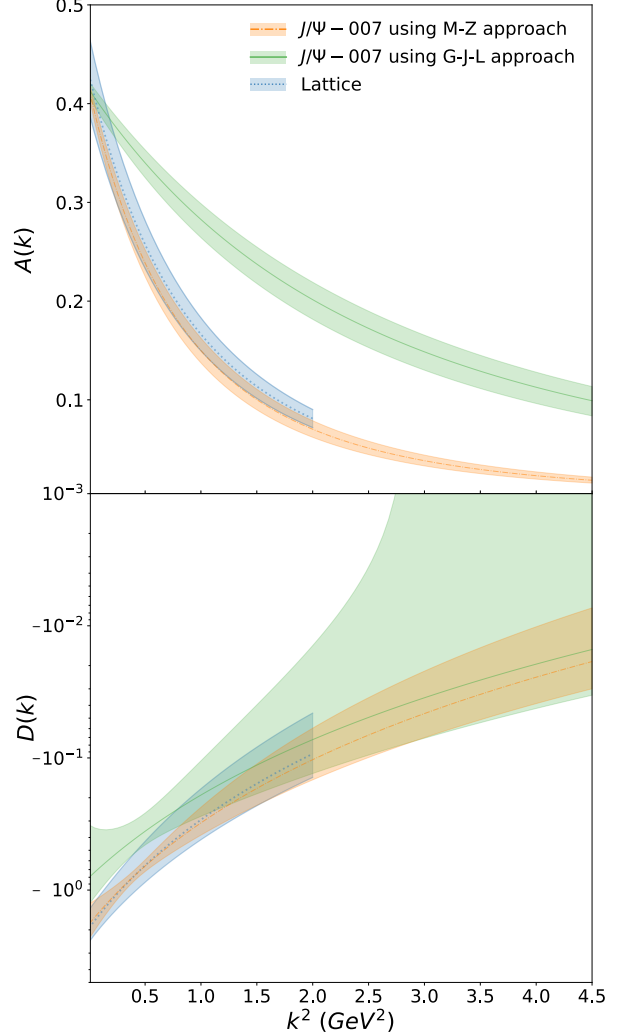


Figure 3. Top panel: The $A_g(k^2)$ form factor extracted from our two-dimensional cross section data in the holographic QCD approach²³ (orange dash-dot curve) and in the GPD+VMD approach¹⁴ (green solid curve), compared to the latest lattice calculation⁹ (blue dotted curve). All form factors used the tripole approximation form. The shaded areas show the corresponding uncertainty bands. Bottom panel: The extracted $D_g(k^2) = 4C_g(k^2)$ form factor with the same color scheme as the top panel. Note the good agreement between the GFFs from the holographic QCD extraction and the lattice results.

to lattice QCD⁹ and find a very good agreement when we follow the holographic QCD approach. Using our results, we derived in each approach the proton mass radius and scalar radius, finding the proton mass radius to be smaller than its charge radius. Furthermore, the holographic QCD extraction yields a scalar radius of one fermi, substantially larger than the charge radius. This compels us to see the proton's structure as consisting of three distinct regions. An inner core, dominated by the tensor gluonic field structure, provides

Table 1. Gluonic GFF parameters and corresponding proton mass and scalar radii, determined from our data through a two-dimensional fit following the holographic QCD and the GPD+VMD approach, compared to the latest lattice results⁹. In all cases we used the tripole-tripole functional form approximation for the GFFs. Note the similar χ^2/ndf in both cases.

Theoretical approach GFF functional form	$\chi^2/\text{n.d.f}$	m_A (GeV 2)	m_C (GeV 2)	$C_g(0)$	$\sqrt{\langle r_m^2 \rangle}$ (fm)	$\sqrt{\langle r_s^2 \rangle}$ (fm)
Holographic QCD Tripole-tripole	0.925	1.575 ± 0.059	1.12 ± 0.21	-0.45 ± 0.132	0.755 ± 0.035	1.069 ± 0.056
GPD + VMD Tripole-tripole	0.924	2.71 ± 0.19	1.28 ± 0.50	-0.20 ± 0.11	0.472 ± 0.042	0.695 ± 0.071
Lattice Tripole-tripole		1.641 ± 0.043	1.07 ± 0.12	-0.483 ± 0.133	0.7464 ± 0.025	1.073 ± 0.066

most of the proton's mass. The charge radius, determined by the relativistic motion of the quarks, extends beyond this inner core. The entirety of the proton is enveloped in a confining scalar gluon density, extending well beyond the charge radius.

References

1. G. Baym, A. Aprahamian et al. An Assessment of U.S.-Based Electron-Ion Collider Science. Available at <https://www.nap.edu/read/25171>, DOI: [10.17226/25171](https://doi.org/10.17226/25171) (2018).
2. Zyla, P. A. et al. Review of Particle Physics. *Prog. Theor. Exp. Phys.* **2020**, 083C01 (2020).
3. Shifman, M. A., Vainshtein, A. I. & Zakharov, V. I. QCD and Resonance Physics. Theoretical Foundations. *Nucl. Phys. B* **147**, 385–447, DOI: [10.1016/0550-3213\(79\)90022-1](https://doi.org/10.1016/0550-3213(79)90022-1) (1979).
4. Shifman, M. A., Vainshtein, A. I. & Zakharov, V. I. QCD and Resonance Physics: Applications. *Nucl. Phys.* **B147**, 448–518, DOI: [10.1016/0550-3213\(79\)90023-3](https://doi.org/10.1016/0550-3213(79)90023-3) (1979).
5. Shifman, M. A., Vainshtein, A. I. & Zakharov, V. I. Remarks on Higgs Boson Interactions with Nucleons. *Phys. Lett.* **78B**, 443–446, DOI: [10.1016/0370-2693\(78\)90481-1](https://doi.org/10.1016/0370-2693(78)90481-1) (1978).
6. Xiong, W. et al. A small proton charge radius from an electron–proton scattering experiment. *Nature* **575**, 147–150, DOI: [10.1038/s41586-019-1721-2](https://doi.org/10.1038/s41586-019-1721-2) (2019).
7. Pagels, H. Energy-Momentum Structure Form Factors of Particles. *Phys. Rev.* **144**, 1250–1260, DOI: [10.1103/PhysRev.144.1250](https://doi.org/10.1103/PhysRev.144.1250) (1966).
8. Teryaev, O. V. Gravitational form factors and nucleon spin structure. *Front. Phys. (Beijing)* **11**, 111207, DOI: [10.1007/s11467-016-0573-6](https://doi.org/10.1007/s11467-016-0573-6) (2016).
9. Pefkou, D. A., Hackett, D. C. & Shanahan, P. E. Gluon gravitational structure of hadrons of different spin. *Phys. Rev. D* **105**, 054509, DOI: [10.1103/PhysRevD.105.054509](https://doi.org/10.1103/PhysRevD.105.054509) (2022). [2107.10368](https://arxiv.org/abs/2107.10368).
10. Wilson, K. G. Confinement of Quarks. *Phys. Rev. D* **10**, 2445–2459, DOI: [10.1103/PhysRevD.10.2445](https://doi.org/10.1103/PhysRevD.10.2445) (1974).
11. Durr, S. et al. Ab-Initio Determination of Light Hadron Masses. *Science* **322**, 1224–1227, DOI: [10.1126/science.1163233](https://doi.org/10.1126/science.1163233) (2008). [0906.3599](https://arxiv.org/abs/0906.3599).
12. Borsanyi, S. et al. Ab initio calculation of the neutron-proton mass difference. *Science* **347**, 1452–1455, DOI: [10.1126/science.1257050](https://doi.org/10.1126/science.1257050) (2015). [1406.4088](https://arxiv.org/abs/1406.4088).
13. Kharzeev, D. E. Mass radius of the proton. *Phys. Rev. D* **104**, 054015, DOI: [10.1103/PhysRevD.104.054015](https://doi.org/10.1103/PhysRevD.104.054015) (2021). [2102.00110](https://arxiv.org/abs/2102.00110).
14. Guo, Y., Ji, X. & Liu, Y. QCD Analysis of Near-Threshold Photon-Proton Production of Heavy Quarkonium. *Phys. Rev. D* **103**, 096010, DOI: [10.1103/PhysRevD.103.096010](https://doi.org/10.1103/PhysRevD.103.096010) (2021). [2103.11506](https://arxiv.org/abs/2103.11506).
15. Hatta, Y. & Yang, D.-L. Holographic J/ψ production near threshold and the proton mass problem. *Phys. Rev. D* **98**, 074003, DOI: [10.1103/PhysRevD.98.074003](https://doi.org/10.1103/PhysRevD.98.074003) (2018). [1808.02163](https://arxiv.org/abs/1808.02163).
16. Hatta, Y., Rajan, A. & Yang, D.-L. Near threshold J/ψ and Υ photoproduction at JLab and RHIC. *Phys. Rev. D* **100**, 014032, DOI: [10.1103/PhysRevD.100.014032](https://doi.org/10.1103/PhysRevD.100.014032) (2019). [1906.00894](https://arxiv.org/abs/1906.00894).
17. Mamo, K. A. & Zahed, I. Diffractive photoproduction of J/ψ and Υ using holographic QCD: gravitational form factors and GPD of gluons in the proton. *Phys. Rev. D* **101**, 086003, DOI: [10.1103/PhysRevD.101.086003](https://doi.org/10.1103/PhysRevD.101.086003) (2020). [1910.04707](https://arxiv.org/abs/1910.04707).
18. Ji, X., Liu, Y. & Zahed, I. Mass structure of hadrons and light-front sum rules in the 't Hooft model. *Phys. Rev. D* **103**, 074002, DOI: [10.1103/PhysRevD.103.074002](https://doi.org/10.1103/PhysRevD.103.074002) (2021). [2010.06665](https://arxiv.org/abs/2010.06665).
19. Sun, P., Tong, X.-B. & Yuan, F. Perturbative QCD analysis of near threshold heavy quarkonium photoproduction at large momentum transfer. *Phys. Lett. B* **822**, 136655, DOI: [10.1016/j.physletb.2021.136655](https://doi.org/10.1016/j.physletb.2021.136655) (2021). [2103.12047](https://arxiv.org/abs/2103.12047).

20. Ji, X. & Liu, Y. Quantum anomalous energy effects on the nucleon mass. *Sci. China Phys. Mech. Astron.* **64**, 281012, DOI: [10.1007/s11433-021-1723-2](https://doi.org/10.1007/s11433-021-1723-2) (2021). [2101.04483](https://arxiv.org/abs/2101.04483).
21. Ji, X. Proton mass decomposition: naturalness and interpretations. *Front. Phys. (Beijing)* **16**, 64601, DOI: [10.1007/s11467-021-1065-x](https://doi.org/10.1007/s11467-021-1065-x) (2021). [2102.07830](https://arxiv.org/abs/2102.07830).
22. Duran, B. *The J/ψ -007 Experiment: A Search for the LHCb Charm Pentaquarks in Hall C at Jefferson Lab.* Ph.D. thesis, Temple University (2021).
23. Mamo, K. A. & Zahed, I. J/ψ near threshold in holographic QCD: A and D gravitational form factors. (2022). [2204.08857](https://arxiv.org/abs/2204.08857).
24. Mamo, K. A. & Zahed, I. Nucleon mass radii and distribution: Holographic QCD, Lattice QCD and GlueX data. *Phys. Rev. D* **103**, 094010, DOI: [10.1103/PhysRevD.103.094010](https://doi.org/10.1103/PhysRevD.103.094010) (2021). [2103.03186](https://arxiv.org/abs/2103.03186).
25. Hou, T.-J. *et al.* New CTEQ global analysis of quantum chromodynamics with high-precision data from the LHC. *Phys. Rev. D* **103**, 014013, DOI: [10.1103/PhysRevD.103.014013](https://doi.org/10.1103/PhysRevD.103.014013) (2021). [1912.10053](https://arxiv.org/abs/1912.10053).
26. Alexandrou, C. *et al.* Complete flavor decomposition of the spin and momentum fraction of the proton using lattice QCD simulations at physical pion mass. *Phys. Rev. D* **101**, 094513, DOI: [10.1103/PhysRevD.101.094513](https://doi.org/10.1103/PhysRevD.101.094513) (2020). [2003.08486](https://arxiv.org/abs/2003.08486).
27. Yang, Y.-B. *et al.* Proton Mass Decomposition from the QCD Energy Momentum Tensor. *Phys. Rev. Lett.* **121**, 212001, DOI: [10.1103/PhysRevLett.121.212001](https://doi.org/10.1103/PhysRevLett.121.212001) (2018). [1808.08677](https://arxiv.org/abs/1808.08677).
28. Shanahan, P. E. & Detmold, W. Gluon gravitational form factors of the nucleon and the pion from lattice QCD. *Phys. Rev. D* **99**, 014511, DOI: [10.1103/PhysRevD.99.014511](https://doi.org/10.1103/PhysRevD.99.014511) (2019). [1810.04626](https://arxiv.org/abs/1810.04626).
29. Hatta, Y., Rajan, A. & Tanaka, K. Quark and gluon contributions to the QCD trace anomaly. *JHEP* **12**, 008, DOI: [10.1007/JHEP12\(2018\)008](https://doi.org/10.1007/JHEP12(2018)008) (2018). [1810.05116](https://arxiv.org/abs/1810.05116).
30. Ali, A. *et al.* First Measurement of Near-Threshold J/ψ Exclusive Photoproduction off the Proton. *Phys. Rev. Lett.* **123**, 072001, DOI: [10.1103/PhysRevLett.123.072001](https://doi.org/10.1103/PhysRevLett.123.072001) (2019). [1905.10811](https://arxiv.org/abs/1905.10811).
31. Bosted, P. E. & Christy, M. E. Empirical fit to inelastic electron-deuteron and electron-neutron resonance region transverse cross-sections. *Phys. Rev. C* **77**, 065206, DOI: [10.1103/PhysRevC.77.065206](https://doi.org/10.1103/PhysRevC.77.065206) (2008). [0711.0159](https://arxiv.org/abs/0711.0159).
32. Gryniuk, O., Joosten, S., Meziani, Z.-E. and Vanderhaeghen, M. Υ photoproduction on the proton at the Electron-Ion Collider (Appendix A). *Phys. Rev. D* **102**, 014016, DOI: [10.1103/PhysRevD.102.014016](https://doi.org/10.1103/PhysRevD.102.014016) (2020). [2005.09293](https://arxiv.org/abs/2005.09293).
33. D'Agostini, G. A Multidimensional unfolding method based on Bayes' theorem. *Nucl. Instrum. Meth. A* **362**, 487-498, DOI: [10.1016/0168-9002\(95\)00274-X](https://doi.org/10.1016/0168-9002(95)00274-X) (1995).
34. Pauk, V. & Vanderhaeghen, M. Lepton universality test in the photoproduction of e^-e^+ versus $\mu^-\mu^+$ pairs on a proton target. *Phys. Rev. Lett.* **115**, 221804, DOI: [10.1103/PhysRevLett.115.221804](https://doi.org/10.1103/PhysRevLett.115.221804) (2015). [1503.01362](https://arxiv.org/abs/1503.01362).
35. Wang, R., Kou, W., Xie, Y.-P. & Chen, X. Extraction of the proton mass radius from the vector meson photoproductions near thresholds. *Phys. Rev. D* **103**, L091501, DOI: [10.1103/PhysRevD.103.L091501](https://doi.org/10.1103/PhysRevD.103.L091501) (2021). [2102.01610](https://arxiv.org/abs/2102.01610).
36. He, F., Sun, P. & Yang, Y.-B. Demonstration of the hadron mass origin from the QCD trace anomaly. *Phys. Rev. D* **104**, 074507, DOI: [10.1103/PhysRevD.104.074507](https://doi.org/10.1103/PhysRevD.104.074507) (2021). [2101.04942](https://arxiv.org/abs/2101.04942).
37. Kharzeev, D. Quarkonium interactions in QCD. *Proc. Int. Sch. Phys. Fermi* **130**, 105–131, DOI: [10.3254/978-1-61499-215-8-105](https://doi.org/10.3254/978-1-61499-215-8-105) (1996). [nucl-th/9601029](https://arxiv.org/abs/hep-th/9601029).
38. Kharzeev, D., Satz, H., Syamtomov, A. & Zinovjev, G. J/ψ photoproduction and the gluon structure of the nucleon. *Eur.Phys.J.* **C9**, 459–462, DOI: [10.1007/s100529900047](https://doi.org/10.1007/s100529900047) (1999). 8 pages, latex, 4 figures Report no: BI-TP 98/36, [hep-ph/9901375](https://arxiv.org/abs/hep-ph/9901375).
39. Wang, R., Evslin, J. & Chen, X. The origin of proton mass from J/Ψ photo-production data. *Eur. Phys. J. C* **80**, 507, DOI: [10.1140/epjc/s10052-020-8057-9](https://doi.org/10.1140/epjc/s10052-020-8057-9) (2020). [1912.12040](https://arxiv.org/abs/1912.12040).
40. Ji, X.-D. A QCD analysis of the mass structure of the nucleon. *Phys. Rev. Lett.* **74**, 1071–1074, DOI: [10.1103/PhysRevLett.74.1071](https://doi.org/10.1103/PhysRevLett.74.1071) (1995). [hep-ph/9410274](https://arxiv.org/abs/hep-ph/9410274).

Methods

An in-depth overview of the experimental methodology for this work can be found in ref.²².

Design

We used the Hall C spectrometers, shown in Fig. 1(c), in four complimentary configurations (see Table 2), to measure and identify charged particles. The detector packages of each spectrometer comprises two sets of identical drift chambers for tracking purposes, two pairs of XY-plane hodoscopes, a threshold Cherenkov counter, and an electromagnetic calorimeter consisting of a pre-shower and a shower unit. The hodoscopes are used as the trigger in each spectrometer. The single-particle trigger rate for each spectrometer varied from 10 to 200 KHz depending on the central angle and momentum settings of the spectrometers. The coincidence trigger is formed by the overlap of the SHMS and HMS single-particle triggers within a narrow time window. The time resolution of the hodoscopes was sufficient to resolve the 2 ns beam bunch structure. Since the single-particle trigger did not include particle identification, we measured a

combination of electrons (positrons), muons, and charged pions in both spectrometers. The coincidence trigger collected the e^+e^- decay pairs from the photoproduced J/ψ s and the combinatoric background from e^-h^+ and h^-h^+ coincidence events. In turn, this enabled the the simultaneous measurement of the background contributions to the J/ψ mass peak. Furthermore, the data include $\mu^+\mu^-$ decay pairs data from photoproduced J/ψ s; the results from this measurement will be described in a separate publication.

Reconstruction

We selected electrons with the SHMS using the electromagnetic calorimeter and positrons with the HMS using the Cherenkov counter and electromagnetic calorimeter. We reconstructed the particle momenta and positions at the interaction vertex from the positions and angles determined at the spectrometer focal plane, measured with two sets of drift chambers, using the optical properties of the spectrometers. We corrected for tracking inefficiencies in each spectrometer as a function of the spectrometer's trigger rate. To account for the computer and electronics live, we used the Hall C electronics dead time monitoring system (EDTM), where a fixed frequency pulse is inserted in the HMS and SHMS trigger logic to mimic real pre-triggers signals. This resulted in a rate-dependent EDTM correction. We also considered and corrected for the effect of target density loss due to temperature fluctuations in the liquid hydrogen target. Finally, due to the low positron rate in the HMS compared to the positive hadron rates, it was necessary to use a different reaction to study the efficiency of the coincidence measurement between both spectrometers. This was possible using $e^-\pi^+$ background events. We instituted a rate-dependent correction based on the measured inefficiencies for these events.

We determined both spectrometer acceptances using a forward single-arm Monte-Carlo simulation (SAMC²²), accounting for the target geometry, spectrometer optics, and detector resolutions (including effects due to internal and external radiative effects the electrons and positrons suffered along their path before and after the interaction point). The simulation used the empirical fit³¹ to world eA inclusive cross section data (using the fit designated as "F1F2-21"). In the kinematic region of our inclusive ep calibration data, the empirical fit has a systematic uncertainty of 3%. The HMS has been used for many experiments in Hall C over the past 30 years, so the acceptance is well understood. The SHMS was installed in Hall C in 2017 and understanding of its acceptance is ongoing. We found that in the central region of momentum and target position, the data and simulation agreed well, while we observed larger disagreements at the edges, with smooth dependence on momentum and target position. We corrected for this with a momentum and position dependent acceptance factor. Finally, we calibrated the central momentum and angles of the spectrometers by measuring elastic scattering on the hydrogen target.

We were able to cleanly measure the J/ψ invariant mass

spectra by combining the event selection criteria described above with a strict timing requirement based on the trigger time and the travel time of the decay leptons from the target to the detectors. Due to the relatively large angles of the spectrometers and the good experimental resolution, the invariant mass peaks are very prominent against a low background. Contamination of the invariant mass spectra from $e^-\pi^+$ is the dominant physics background. We were able to precisely determine the background shape through our direct measurement of these events, where we fixed the background normalization to the side bands of the invariant lepton pair mass spectrum. After background subtraction, we obtained the raw J/ψ cross section by integrating the remaining spectrum over a fixed window around the J/ψ invariant mass, as a function of the photon energy E_γ and Mandelstam variable t .

The observed raw J/ψ cross section consist of events from bremsstrahlung photons and quasi-real photons from the electron beam, interacting with either the liquid hydrogen target or with the aluminum target walls. We corrected for the target wall contributions based on measurements with a two-aluminum-foil target. To account for contributions from quasi-real events we determined the fraction of electroproduction events to photoproduction events using the 1Ager Monte Carlo generator³² and a full simulation of the experimental setup. We then unfold for radiative effects on the J/ψ decay, limited detector resolution and acceptance, the bremsstrahlung photon flux, and the J/ψ branching ratio through an iterative unfolding approach³³ using two Monte-Carlo samples. The resulting Born-level photoproduction cross section for each of the experimental settings is differential in t as a function of E_γ .

Backgrounds

Since we did not detect the recoil proton, the degree of exclusivity of the reaction was aided by its near-threshold kinematics and the narrow acceptance of the spectrometers. Background events, where an extra pion is produced with the J/ψ in the range of available photon energies would fall outside the kinematic settings for the elastic J/ψ production and would reconstruct below t_{\min} , however, these type of events were not observed in our data sample. Another background we investigated in our kinematics settings is the Bethe-Heitler process. This background was evaluated according to ref.³⁴ and found to be small (< 1%) due to the combined spectrometers very limited acceptance and large spectrometer angles. This is consistent with the lack of an observed shoulder in the e^+e^- invariant mass spectrum.

Systematic Uncertainties

The systematic uncertainties on our two-dimensional cross section consist of two parts: an overall 4% scale uncertainty and an additional point-to-point uncertainty. The point-to-point uncertainties are in all cases significantly smaller than the statistical uncertainties. Finally, we investigated bin-to-bin correlations due to the unfolding procedure, and found

the effect to be negligible.

The scale uncertainty is mainly driven by the 3% uncertainty on the F1F2-21 DIS model we used to calibrate our detector acceptance. Other major contributions to the scale uncertainty are due the correction for residual rate dependence (1.2%), to the luminosity measurement (1%), residual correction to the SHMS acceptance based on the vertex position (1%), target window subtraction (1%), subtraction of electroproduction events (1%), radiator thickness (1%), detector life time correction (0.45%), tracking efficiency correction (0.44%), target boiling correction (0.44%). The systematic uncertainty due to particle identification inefficiencies was also considered and found to be negligible.

We considered the following sources to estimate the point-to-point systematic uncertainties: to estimate the uncertainties due to the background subtraction on the invariant mass, the radiative corrections, and the material effects we conducted the entire cross section analysis with varying integration windows on the invariant mass spectrum, varying between very narrow (cutting out the tail on the J/ψ invariant mass peak), and very wide. The maximum absolute difference between the different variant analysis was taken as the contribution to the systematic uncertainty. To estimate the dependence of the unfolding procedure on the Monte-Carlo model, we repeated the approach with two very different models: a two-gluon model fit to the world data excluding GlueX and assuming s -channel helicity conservation, and the a different model from the JPAC group which includes the recent GlueX results and uses a full description of the spin-density matrix elements to describe the J/ψ polarization. The difference between both models was taken as systematic uncertainty. To obtain the total systematic uncertainty we added both contributions in quadrature.

Additional information

Kinematic settings

In Table 2 we summarize each kinematic setting. We list the spectrometers momentum and angle settings and their corresponding t and E_γ regions.

Table 2. Spectrometers polarity, momentum and angle settings for $J/\psi - 007$ experimental measurements.

Settings	HMS (+)	SHMS (-)
Setting 1	4.95 GeV, 19.1°	4.835 GeV, 17.0°
Setting 2	4.6 GeV, 19.9°	4.3 GeV, 20.1°
Setting 3	4.08 GeV, 16.4°	3.5 GeV, 30.0°
Setting 4	4.4 GeV, 16.5°	4.4 GeV, 24.5°

Interpretation in the DK approach

In the case of DK approach, we extracted the mass radius first. To this end we fitted our t dependent differential cross sections and extracted the radius at each photon energy fol-

lowing ref.¹³ prescription's

$$\frac{d\sigma}{dt} = \frac{1}{64\pi s} \frac{1}{|p_{\gamma cm}|^2} (Q_e c_2)^2 \left(\frac{16\pi^2 M^2}{b} \right)^2 G(t)^2 \quad (3)$$

where M is the nucleon mass, $p_{\gamma cm}$ is the center of mass photon momentum Q_e the electric charge of the charm quark ($Q_e = 2e/3$), c_2 is a short distance coefficient, determined from the fit and $b = 11 - 2n_l/3 - 2n_h/3 = 9$ with n_l and n_h the number of light and heavy quarks respectively. Here one effective scalar GFF of a dipole form, $G(t) = M(1 - t/m_s^2)^{-2}$ is used with $G(0) = M$ in the rest frame of the particle. It encompasses a combination of the three GFFs, $A_g(t)$, $B_g(t)$ and $C_g(t)$ of the standard decomposition of the energy-momentum tensor in a nucleon state. The proton mass radius is then given according to ref.¹³ by,

$$\langle r_m^2 \rangle = \frac{6}{M} \frac{dG}{dt} \Big|_{t=0} = \frac{12}{m_s^2} \quad (4)$$

The extracted mass radii at different photon energies, according to this prescription, are shown in Fig.4 (left). At higher energies, an energy independent region of radii consistent with GlueX emerges, however, we see a decrease in the size of the extracted radius as we get closer to the threshold,

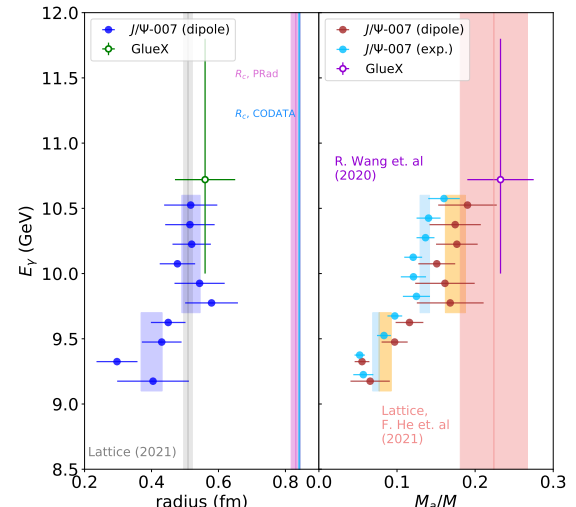


Figure 4. Left panel: The extracted radius as a function of the photon energy according to Ref.¹³ together with the GlueX result. Both our and the GlueX extractions used a dipole fit of the form factor. The charge radius from CODATA and the latest electron scattering⁶ (labeled PRAD) are plotted as lines with error bands. The lattice result is plotted as a grey line with grey error band. Right panel: The extracted M_a/M according to Ji's mass decomposition⁴⁰ following³⁹ along with a recent direct lattice calculation of the same quantity³⁶.

below 9.7 GeV. The radius determined in the energy independent region averages to $\sqrt{\langle r_m^2 \rangle} = 0.52 \pm 0.03$ fm. This result

Table 3. Using the DK approach the table shows the mass radii at each photon energy according to DK¹³ and the trace anomaly similar to³⁹.

E_γ (GeV)	m_A (GeV)	c_2 (nb/GeV 2) $^{\frac{1}{2}}$	$\chi^2/n.d.f$	Mass radius (fm)	M_a/M (dipole)	M_a/M (exp.)
9.10-9.25	1.69 ± 0.45	34.10 ± 10.60	0.45	0.404 ± 0.107	0.066 ± 0.025	0.057 ± 0.013
9.25-9.40	2.30 ± 0.47	27.37 ± 4.30	0.96	0.297 ± 0.061	0.055 ± 0.009	0.052 ± 0.007
9.40-9.55	1.59 ± 0.22	46.34 ± 7.35	0.89	0.430 ± 0.059	0.097 ± 0.017	0.083 ± 0.009
9.55-9.70	1.52 ± 0.17	53.57 ± 7.63	0.39	0.450 ± 0.052	0.116 ± 0.018	0.097 ± 0.009
9.70-9.85	1.18 ± 0.16	75.39 ± 16.88	0.49	0.579 ± 0.079	0.168 ± 0.043	0.125 ± 0.017
9.85-10.00	1.26 ± 0.17	70.06 ± 14.65	0.85	0.544 ± 0.075	0.161 ± 0.038	0.121 ± 0.016
10.00-10.15	1.43 ± 0.16	63.75 ± 9.24	1.20	0.477 ± 0.053	0.151 ± 0.024	0.121 ± 0.011
10.15-10.30	1.31 ± 0.14	72.74 ± 10.20	2.01	0.520 ± 0.057	0.177 ± 0.027	0.136 ± 0.011
10.30-10.45	1.33 ± 0.19	70.29 ± 12.07	0.48	0.515 ± 0.074	0.174 ± 0.033	0.140 ± 0.015
10.45-10.6	1.32 ± 0.20	75.32 ± 13.59	0.74	0.517 ± 0.079	0.190 ± 0.038	0.160 ± 0.020

compares favorably with the lattice QCD determination of the radius using solely the $A_g(t)$ gluonic GFF of^{9,28} and equation (4). We observe that in¹³ approach the mass radius is clearly smaller than the charge radius of the proton.

In Table 3 we list the fit parameters and the corresponding uncertainties in the approach of Ref.¹³. From those parameters we extract the radius according to¹³ and the anomalous energy contribution⁴⁰ to the proton mass according to³⁹.

Moreover, following the same procedure described in ref.³⁹, based also on^{13,37,38} assuming a dilaton (0^{++}) scalar exchange between the J/ψ and the nucleon, we inferred the quantum anomalous energy discussed in ref.²¹. The results are shown in the right panel of Fig. 4. We extracted M_a/M using both an exponential GFF as in Ref.³⁹ as well as a dipole form GFF as in ref.¹³. We used the energy independent region to determine an average value and find $M_a/M = 0.175 \pm 0.013$. Of course, this quantity should be energy independent but clearly it is not as we consider photon energies smaller than 9.7 GeV and thus raises the question about the validity of its interpretation. Nevertheless, it is interesting that the dipole form factor extraction is closer to the first direct lattice calculation³⁶ of the same quantity and offers a glimpse on the origin of the proton mass.

Data availability

The raw data from the experiment are archived in Jefferson Laboratory mass storage silo and at Argonne National Laboratory. The analyzed data are archived at Argonne National Laboratory. The data are available from the authors upon request.

Acknowledgements

This work was supported in part by the US Department of Energy Office of Science, Office of Nuclear Physics under contracts numbers DEAC02- 06CH11357 and DE-FG02-94ER40844, including contract number DE-AC05-06OR23177, under which Jefferson Science Associates, LLC operates the Thomas Jefferson National Accelerator Facility.

Author contributions

S. J., M.K. J., Z.-E. M., M. P., and E. C. are co-spokespersons of the experiment. The data analysis was carried by B. D, S. J., M. K. J., S. P., C. P., and Z.-E. M. All authors reviewed the manuscript. The entire J/ψ -007 collaboration participated in the data collection and in the on-line analysis of the experiment.

Accession codes (where applicable):

Competing interests (man. The authors declare no competing interests.

Supplementary information

Supplementary information is available for this paper in the form of Extended Data figures and tables.

Correspondence and request of materials

Correspondence and request of materials should be addressed to Z.-E.M.